UAV-based mapping, back analysis and trajectory modelling of a co-seismic rockfall in Lefkada Island, Greece

Charalampos Saroglou[1*],

Pavlos Asteriou[1]

Dimitrios Zekkos[2]

George Tsiambaos[1]

Marin Clark[3]

John Manousakis[4]

[1]Department of Geotechnical Engineering, School of Civil Engineering, National Technical University of Athens

[2]Department of Civil and Environmental Engineering, University of Michigan, USA

[3]Department of Earth and Environmental Science, University of Michigan, USA

[4]Elxis Group, S.A, Athens, Greece

* corresponding author: saroglou@central.ntua.gr

Abstract

We present field evidence and kinematic study of rock block motion mobilised in the Ponti area by an M_w 6.5 earthquake near the island of Lefkada on 17th November 2015. A detailed survey was conducted using an Unmanned Aerial Vehicle (UAV) with an ultra-high definition (UHD) camera, which produced a high-resolution orthophoto and a Digital Surface Model (DSM) of the terrain. The sequence of impact marks from the rock trajectory on the ground surface was identified from the orthophoto and field verified. Additionally, calculation of earthquake characteristics defined the acceleration of the rock slope and the initial condition of the detached block. Using the impact points from the measured rockfall trajectory, an analytical reconstruction of the trajectory was developed, which led to insights on the coefficients of restitution. The measured trajectory was compared with modeled rockfall trajectories using recommended

parameters. However, the actual trajectory could not be accurately predicted, revealing limitations of existing models.

Keywords

Rockfall, earthquake, DEM, modelling, restitution, UAV

1. Introduction

Active faulting, rock fracturing and high rates of seismicity contribute to common rockfall hazards in Greece. Rockfalls primarily damage roadways and houses (Saroglou, 2013) and are most often triggered by rainfall and secondly seismic loading. Additionally in recent years, some rockfalls have impacted archaeological sites (Marinos & Tsiambaos, 2002, Saroglou et al., 2012). The Ionian Islands, which include Lefkada Island, experience frequent M_w 5-6.5 earthquakes, as well as less frequent larger (up to 7.5) earthquakes. The historical seismological record is particularly well constrained with reliable detailed information for at least 23 such earthquake events since 1612 that induced ground failures at the island of Lefkada. On average, Lefkada experiences a damaging earthquake every 18 years. In the recent past, a M_w 6.2 earthquake occurred on August 14 2003 offshore the NW coast of Lefkada, and caused landslides, rockslides and rockfalls along the western coast of the island (Karakostas et al. 2004, Papathanasiou et al., 2012). Significant damage was reported, particularly in the town of Lefkada, where a PGA of 0.42g was recorded.

On November 17th 2015, an M_w 6.5 earthquake again struck the island of Lefkada and triggered a number of landslides, rockfalls and some structural damage. The most affected area by large rockslides was the western coast of the island, especially along its central and south portion, which are popular summer tourist destinations (Zekkos et al., 2017). The coseismic landslides completely covered the majority of the west coast beaches and damaged access roads.

On the southeast side of Lefkada near the Gulf of Vassiliki, a seismically-triggered rockfall in Ponti village was responsible for one of two deaths caused by the earthquake (Figure 1). Of particular interest, is the very long travel path of the rock block, which was about 800 m in plan view from the point of detachment to the end of its path. Near the end of the rock fall path, the block impacted a family residence, penetrated two brick walls and killed a person in the house. The block exited through the back of the house and came to rest in the property's backyard.

The Ponti village rockfall site is characteristic of earthquake induced rockfall and an example of how seismically-induced rockfall impacts human activities. It also provides an opportunity to evaluate 2D and 3D rockfall analysis to predict details of the rockfall trajectory, basd on measured by field evidence. In order to create a highly accurate model of the rockfall propagation in 2D and 3D space, the rock path and the impact point on the slope was identified by a field survey. The study was performed using an Unmanned Aerial Vehicle (UAV) with an ultra-high definition (UHD) camera, which produced a high-resolution orthophoto and a Digital Surface Model (DSM) of the terrain. The orthophoto was used to identify the rolling section and the bouncing points of the rock along its trajectory, which were verified by field observation. The high-resolution DSM made it possible to conduct kinematical rebound analysis and a 3D rockfall analysis.

2. Ponti rockfall - site conditions

The locations of the epicenters of the 2003 and 2015 events, as well as the location of the rockfall study site are shown in Figure 1. The southwest coast of Lefkada is part of the Triassic to Eocene age Paxos zone and consists of limestones and dolomites that are covered by Neogene clastic sedimentary rocks, mostly sandstones and marls. Figure 1 also shows faults and high rockfall hazard areas as identified by Rondoyanni et al. (2007). The rockfall at Ponti is not located in a high rockfall hazard area. Based on measurements conducted at one location along the rockfall path using the

Multichannel Analysis of Surface Waves method, the in-situ shear wave velocity of the top layer was estimated to be around 800 m/sec, which is a high velocity and consistent with the rock conditions expected at the site.

The slope overhanging Ponti village is made of limestone and has a maximum height of 600 m and an average slope angle of 35^0 to 40^0 (Figure 2). The geological formations at the Ponti rockfall site are limestones covered by moderately cemented talus materials. The thickness of the talus materials ranges between 0.5 and 4.0 to 5.0 m. A few fallen limestone blocks were identified on the scree slope, with volumes between 0.5 and 2 m^3. Based on the size distribution of these rocks on the slope, the average expected block volume would be in the order of 1 to 2 m^3.

The rockfall release area was at an elevation of 500 m, while the impacted house at an elevation of 130 m (Figure 3). The volume of the detached limestone block was approximately 2 m^3 and its dimensions equal to 1.4 m x 1.4 m x 1 m. There was no previous rockfall incident reported for the specific slope that impacted the road or house.

3. UAV mapping

3.1. Introduction

A quadrotor UAV (Phantom 3 professional) was deployed to reach the uphill terrrain that was practically inaccessible. The UAV was equiped with an Ultra-high definition (UHD) 12 MP camera and had the capacity to collect 4K video. The sensor was a 1/2.3” CMOS (6.47x3.41mm) and the effective pixel resolution was 12.4 MP (4096x2160 pixels). An immediate UAV data acquisition expedition was conducted 2 days after the earthquake. A second more detailed mapping UAV expedition with the objective to create a DEM was conducted 5 months after the rockfall event.

The first objective of the UAV deployment was to find the inititiation point of the rock and then identify the rockfall path (shown in Figure 2). A particular focus on that part of the task was the identification of rolling and bouncing sections of the rockfall path. In addition, in order to generate a high-resolution orthophoto of the rockfall trajectory, aerial video imagery was collected, and the resulting digital surface model (DSM) was used to perform rockfall analysis.

The Structure-from-Motion (SfM) methodology wase implemented to create a 3D point cloud of the terrain and develop a 3D model. The methodology is based on identifying matching features in multiple images, and thus imaery overlap of at least 70% is required. Compared to classic photogrametry methodologies, where the location of the observing point is well established, SfM tracks specific discernible features in multiple images, and through non-linear least-squares minimisation (Westoby et al., 2012), iteratively estimates both camera positions, as well as object coordinates in an arbitrary 3D coordinate system. In this process, sparse bundle adjustment (Snavely et al., 2008) is implemented to transform measured image coordinates to three dimensional points of the area of interest. The outcome of this process is a sparse 3D point cloud in the same local 3D coordinate system (Micheletti et al., 2015). Subsequently, through an incremental 3D scene reconstruction, the 3D point cloud is densified. Paired with GPS measurements of a number of control points (for this site, 10 fast-static GPS points were collected) at the top, middle and bottom of the surveyed area, the 3D point cloud is georeferenced to a specific coordinate system and through post-processing a digital surface model (DSM) or digital terrrain model (DTM) and orthiphotos are created. The SfM methodology was implemented in this study using the Agisoft Photoscan software.

In addition, the accuracy of the model has been examined by using portions of the ground control points and developing DEM of differencing between different models, an investigation that is described in our paper by Manousakis et al. (2016). Finally, a comparison was made of the DEM developed by the UAV against the satellite-based DEM that is part of the Greek cadastre. The two surfaces were found to be very similar.

The overlap between pictures was minimum frontal 80%, side 65% and a total of 714 camera station (video frames extracted) were included as shown in Figure 4.

3.2. High-resolution Orthophoto

A 5cm pixel size orthophoto was generated based on the methodology outlined earlier. As shown in Figure 5, the rolling section and the bouncing locations of the rock block throughout its course were identified. The rolling section was discerned as a continuous and largely linear mark left in the densely vegetated terrain that was indicative of the damage caused. Impact points that are part of the bouncing section of the rock, were identified as circular to ellipsoidal bare earth craters with no disturbance in between. The last bouncing point before impacting the house is clearly identified on the paved road. The plan view ortho-imagery, along with the original footage of the video collected was crucial to the qualitative identification of these features. The alternative, i.e., land-based, conventional field reconnaissance was physically impossible to perform in the densely vegetated and steep terrain.

3.3. Digital Surface Model

A profile section and a 10 cm Digital Surface Model (DSM) paired with the plan view orthophoto were first developed (Manousakis et al., 2016) allowing the identification of terrain features such as structures, slope benches or high trees, which could affect the rock's path downhill. However, this resolution of the DSM proved to be not only unnecessarily high and thus difficult to manipulate in subsequent rockfall analyses, but also resulted in numerical instabilities during the rockfall analyses. Therefore, a downscaled 2 m DSM was produced for the rockfall analysis. This was implemented through an aggregate generalization scheme where each output cell is assigned the minimum of the input cells that are encompassed by that cell. In addition, noise filtering and smoothing processing were implemented to reduce the effect of construction elements and vegetation in the final rasterized model. Note that this resolution is still higher than the resolution of DSM that are often used in rockfall analyses.

Algorithms for vegetation removal were executed within Whitebox GAT Geospatial Analysis Tools platform. GCPs were used for both georeferencing and solving camera’s internal and external parameters. The process involves Point Cloud neighborhood examination and DEM smoothing algorithms. Firstly, a bare-Earth digital elevation model (DEM) was interpolated from the input point cloud LAS file, by specifying the grid resolution (2m) and the inter-point slope threshold. The algorithm distinguished ground points from non-ground points based on the inter-point slope threshold. The interpolation area was divided into grid cells, corresponding to the cells of the output DEM. All of the point cloud points within the circle encompassing each grid cell were then examined as a neighborhood. All points within a neighborhood that have an inter-point slope with any other point and are also situated above the corresponding point, are considered to be a non-ground point. An appropriate value for the inter-point slope threshold parameter depends on the steepness of the terrain, but generally values of 15-35 degrees produce satisfactory results. The elevation assigned to the grid cell was then the nearest ground point elevation (Whitebox GAT help topics).

Further processing of the interpolated bare-earth DEM was introduced to improve vegetation and structures removal results by applying a second algorithm to point cloud DEMs, which frequently contain numerous off-terrain objects such as buildings, trees and other vegetation, cars, fences and other anthropogenic objects. The algorithm works by finding and removing steep-sided peaks within the DEM. All peaks within a sub-grid, with a dimension of the user-specified Maximum Off-Terrain Object (OTO) Size, in pixels, were identified and removed. Each of the edge cells of the peaks were then examined to see if they had a slope that is less than the user-specified Minimum OTO Edge Slope and a back-filling procedure was used. This ensured that OTOs are distinguished from natural topographic features such as hills (Whitebox GAT help topics). Total RMS error after filtering for 6 GCPs was 0.07m, while total RMS error for 4 Check Points was 0.20m. When compared to a 5m DEM from Greek National Cadastre with a geometric accuracy of RMSEz ≤ 2,00m and absolute accuracy ≤ 3,92m for a confidence level of 95%, a mean difference of 0.77 m and a standard deviation of 1.25 m is observed, which is well into the range of uncertainty of the cadastre model itself.

4. Earthquake characteristics – Initial conditions

4.1. Seismic acceleration

The epicenter of the earthquake according to the National Observatory of Athens, Institute of Geodynamics (NOA) is located onshore near the west coast of Lefkada. The causative fault is estimated to be a near-vertical strike-slip fault with dextral sense of motion (Ganas et al., 2015, 2016). Based on the focal mechanism study of the earthquake, it was determined that the earthquake was related to the right lateral Kefalonia-Lefkada Transform Fault (KLTF), which runs nearly parallel to the west coasts of both Lefkada and Kefalonia island, in two segments (Papazachos et al. 1998, Rondoyanni et al. 2012).

A strong motion station recorded the ground motions in the village of Vasiliki located at a distance of 2.5 km from the Ponti rockfall site. The ground motion characteristics of the recording are summarized in Table 1 and are presented in Figure 6, according to an ITSAK preliminary report (ITSAK, 2016).

4.2. Topography effect

Peak ground acceleration along the rock slope is the intensity of base shaking modified by site and topographic effects (Mavrouli et al., 2009). In the present case, local shaking intensity in terms of horizontal PGA was considered. The E-W component of acceleration was considered for the determination of the initial velocity. The peak ground acceleration (PGA) on the slope face (PGA_{sf}) was obtained by linear interpolation between the acceleration at the base (PGA_b) and at the slope crest

(PGA_{cr}). The acceleration at the base was equal to 0.32g and thus at the crest PGA_{cr}= 1.5 PGA_b equal to 0.48g, was estimated at the site of detachment.

4.3. Initial velocity of rock block

The initial horizontal velocity of the block, at the time of detachment, was calculated considering equilibrium of the produced work and the kinetic energy according to equation 1.

$$v_x = \sqrt{2 \times PGA_{sf} \times s} \quad (1),$$

where PGA_{sf} is the acceleration on the slope at the location of detachment and *s* the initial displacement of the block in order to initiate its downslope movement.

The initial horizontal velocity was calculated equal to 0.67 m/sec, considering a displacement in the order of s = 0.05 m. The vertical component of the initial velocity is assumed to be zero.

5. Trajectory analysis

In order to estimate the possible rock paths and design remedial measures, simulation programs based on lumped-mass analysis models are commonly used in design practice. The trajectory of a block is modelled as a combination of four motion types; free falling, bouncing, rolling and sliding (Descoeudres and Zimmermann, 1987). Usage of the lump-mass model has some key limitations; the block is described as rigid and dimensionless with an idealized shape (sphere); therefore the model neglects the block’s actual shape and configuration at impact, even though it is evident that they both affect the resulting motion.

5.1. Modelling the response to an impact

The most critical input parameters are the coefficients of restitution (COR), which control the bouncing of the block. In general, the coefficient of restitution (COR) is defined as the decimal fractional value representing the ratio of velocities (or impulses or energies; depending on the definition used) before and after an impact of two colliding entities (or a body and a rigid surface). When in contact with the slope, the block's magnitude of velocity changes according to the COR value. Hence, COR is assumed to be an overall value that takes into account all the characteristics of the impact; including deformation, sliding upon contact point, transformation of rotational moments into translational and vice versa (Giani, 1992).

The most widely used definitions originate from the theory of inelastic collision as described by Newtonian mechanics. For an object impacting a rocky slope (Figure 7), which is considered as a steadfast object, the kinematic COR (v_{COR}) is defined according to Eq. 2.

$$v_{COR} = \frac{v_r}{v_i} \qquad (2)$$

where v is the velocity magnitude and the subscripts i and r denote the trajectory stage; incident (before impact) and rebound (after impact) respectively.

Two different mechanisms participate in the energy dissipation process; energy loss normal to the slope is attributed to the deformation of the colliding entities, and in the tangential direction is due to friction between them. Therefore kinematic COR has been analyzed to the normal and tangential component with respect to the slope surface, defining the normal (n_{COR}) and the tangential (t_{COR}) coefficient of restitution (Eq. 3 and 4 respectively).

$$n_{COR} = \frac{v_{n,r}}{v_{n,i}} \qquad (3)$$

and

$$t_{COR} = \frac{v_{t,r}}{v_{t,i}} \qquad (4)$$

where the first subscript, n or t denotes the normal or the tangential components of the velocity respectively.

Normal and tangential COR have prevailed in natural hazard mitigation design via computer simulation due to their simplicity. Values for the coefficients of restitution are acquired from values recommended in the literature (Azzoni et al. 1995; Heidenreich 2004; Richards et al. 2001, RocScience, 2004). Those are mainly related to the surface material type and originate from experience, experimental studies or back analysis of previous rockfall events. This erroneously implies that coefficients of restitution are material constants. However, COR values depend on several parameters that cannot be easily assessed. Moreover, the values suggested by different authors vary considerably and are sometimes contradictory.

5.2. Rockfall path characteristics

23 impact points were identified on the slope surface (Figure 8). Their coordinates are presented in Table 2, along block's path starting from the detachment point (where x=0). No trees were observed along the block's path.

The apparent dip of the slope at impact positions was measured from the topographic map; on each impact point a line was set with a length twice the block's mean dimension, oriented according to preceding trajectory direction. Moreover, the impact point was expanded on the topographic map to a rectangular plane with a side twice as much the mean dimension of the block (Figure 9). This plane was then oriented so that one side coincides with the strike direction and its' vertical side toward to the dip direction. Thus, direction difference, $\Delta\varphi$, was measured by the strike direction and the preceding path and deviation, e, was measured as the angle between pre and post impact planes (Asteriou & Tsiambaos, 2016).

Having a detailed field survey of the trajectory path, a back analysis according to the fundamental kinematic principles was performed in order to back-calculate the actual COR values.

5.3. Kinematic analysis and assumptions

The 23 impact points identified on the slope comprise a rockfall path of 22 parabolic segments. The vertical and horizontal length of each segment is acquired by subtracting consecutive points. Since no external forces act while the block is in the air, each segment lays on a vertical plane and is described by the general equation of motion as:

$$y = x \tan \vartheta - \frac{g x^2}{2 v_i^2 \cos^2 \vartheta} \qquad (5)$$

where: θ the launch angle from the horizon and v the launch (initial) velocity (Figure 10).

Since no evidence can be collected regarding launch angle and velocity, innumerable parabolas satisfy Eq. 5. However, θ is bound between –β and 90°, so in order to acquire realistic values for the initial velocity, its sensitivity for that given range was addressed (Figure 11).

For the case presented in Fig. 11 (the first parabolic segment) it is seen that for the majority of the release angles, initial velocity variation is low and ranges between 7.2 and 12 ms^{-1}. Additionally, the relationship between release angle and initial velocity is expressed by a curvilinear function, thus a minimum initial velocity value along with its release angle (denoted hereafter as θ_{cr}) can be easily acquired.

Given the minimum initial velocity and the critical release angle for each parabolic segment, the impact velocity and angle can be calculated. Afterwards, normal and tangential velocity components according to the apparent dip of the impact area, are calculated in order to evaluate COR values. Results are summarized in Table 3.

5.4. Coefficients of restitution

It is observed that v_{cor} (Table 3) is slightly greater than one in 5 out of 22 impacts. According to Eq. 3, this can only be achieved when impact velocity is less than rebound velocity. However, this indicates that energy was added to the block during contact, which is not possible according to the law of conservation of energy. Thus, impact velocity should be greater, which is possible if the launch velocity of the previous impact was more than the assumed minimum.

Omitting the impacts with V_{cor}>1, it is observed that kinematic COR ranges between 0.55 and 1.0 and presents smaller variation compared to normal or tangential coefficient of restitution, similar to what was previously reported in relevant literature (i.e. Asteriou et al, 2012; Asteriou & Tsiambaos, 2016).

The considerably wide scatter of normal COR implies that the restitution coefficient cannot be a material constant. Yet, in most relevant software, normal COR is defined solely by the slope material. Moreover, normal COR values higher than one were calculated in 11 out of the 15 remaining impacts. Normal COR higher than one have been observed in both experimental (e.g. Spadari et al., 2011; Buzzi et al., 2012; Asteriou et al., 2012) and back-analysis studies (e.g. Paronuzzi, 2009) and are related to irregular block shape and slope roughness, as well as to shallow impact angle and angular motion. A more detailed presentation of the reasons why normal COR exceeds unity can be found in Ferrari et al. (2013). However, in relevant software normal COR values are bounded between 0 and 1.

Moreover, it is observed in Figure 12 that normal COR increases as the impact angle reduces, similarly to previous observations by Giacomini et al. (2012), Asteriou et al. (2012) and Wyllie (2014). The correlation proposed by Wyllie (2014) is also plotted in Figure 13 and seems to describe consistently, but on the unconservative side, the trend and the values acquired by the aforementioned analysis and assumptions.

6. Rockfall modelling

6.1. 2-D analyses

Initially, a deterministic 2D rockfall analysis was performed using Rocfall software (RocScience, 2004). According to Asteriou & Tsiambaos (2016) the most important influence is posed by the impact configuration, which is influenced by slope roughness and block shape. In this study, roughness has been fully taken into account (considering the block's dimension scale) by the accurate cross-section used in the analyses (more than 1500 x-y points were used – approximately 2 points per meter). Based on our experience, this accuracy is significantly higher compared to other similar research projects. Moreover, with the available data and the performed lump-mass model analysis, it was not possible to simulate block shape effect nor the configuration of the block at impact.

Considering an initial velocity of 0.67 m/sec, according to the numerical analyses, the falling rock primarily rolls on the slope and stops much earlier than its actual run out distance, approximately 400 m downslope from its starting point (Fig. 8; case 1). The restitution coefficients were n_{COR}=0.35, t_{COR}=0.85, which represent properties of bedrock outcrops according to the suggested values provided in the documentation of the software.

The friction angle was set to zero. A standard deviation for the coefficients of restitution, the friction angle and roughness of the material on the slope was not used, as the analysis was deterministic. If the friction angle is set to $\varphi=32^0$ (as suggested by the software documentation), the rock travels downslope only 50 m.

A separate analysis was performed, with lower coefficients of restitution, resembling that of talus material on the slope (n_{COR}=0.32, t_{COR}=0.82, $\varphi=30^0$) as proposed by the suggested values provided in the documentation of the software. In this case, the rock block rolled only a few meters downslope. Therefore, it is evident that the actual rock trajectory cannot be simulated.

In order to simulate the actual trajectory as much as possible, various combinations of restitution coefficients and friction angle were considered. The closest match occurred for n_{COR}=0.60 and t_{COR}=0.85, while the friction angle was set to zero and no velocity scaling was applied. Only in such an analysis, the rock block reaches the house; with a velocity equal to v=18 m/s approximately (Fig. 8; case 2). According to the suggested values, these values for the coefficients correspond to a bedrock material (limestone).

In this case, the modelled trajectory is significantly different from the actual one. The main difference is that the block is rolling up to 200 m downslope while the actual rolling section is 400 m (as shown in Figure 8). Furthermore the impacts on the ground in the bouncing section of the trajectory are considerably different in number (14 versus 23) and in location from the actual ones. Finally, the bounce height of some impacts seems unrealistically high. For example, the 2nd bounce presents a jump height (f) of ~17.5m over a length (s) of ~50m, resulting to a f/s ratio of ~1/3, when the characteristic f/s ratios for high, normal and shallow jumps is 1/6, 1/8 and 1/12 respectively, as suugested by Volkwein et al. (2011).

6.2. 3-D rockfall analysis

The rockfall trajectory model Rockyfor3D (Dorren, 2012) has also been used in order to validate the encountered trajectory and determine the reach probability of the falling rock (from the specific source area) on the impacted house.

The 3D analysis was based on the down-scaled 2 m resolution Digital Elevation Model (DEM) that was generated from the 10 cm DSM. The terrain features such as low vegetation (e.g. bushes) and the trees were removed from the DEM as they affected the rock's path downhill. The following raster maps were developed for the 3D analysis: a) rock density of rockfall source, b) height, width, length and shape of block, c) slope surface roughness and d) soil type on the slope, which is directly linked with the normal coefficient of restitution, n_{COR}.

The slope roughness was modeled using the mean obstacle height (MOH), which is the typical height of an obstacle that the falling block encounters on the slope at a possibility percentage of 70%, 20% and 10% of the trajectories (according to the suggested procedure in Rockyfor3D). No vegetation was considered in the analysis, which favours a longer trajectory. The parameters considered in the 3D analysis for the different formations are summarised in Table 4. The spatial occurrence of each soil type is shown in Figure 13 and the assigned values of n_{COR} are according to the Rockyfor3D manual. The values for soil type 4.1 in Figure 13 are slightly different from soil type 4 (proposed in the manual), denoting talus with a larger percentage of fallen boulders. The block dimensions were considered equal to 2 m^3 and the shape of the boulder was rectangle. In order to simulate the initial velocity of the falling rock due to the earthquake, an additional initial fall height is considered in the analysis, which for this case was set equal to 0.5 m.

The energy line angles were recalculated from the simulated trajectories and it was determined that the energy line angle with highest frequency (39%) was 30-31^0. Based on the 3D analysis no rock blocks would impact the house, although the rock paths are closer to the actual trajectories compared to RocFall software. The reach probability of the falling rocks, initiating from the source point, is shown in Figure 14.

6.3. Lateral dispersion & Deviation

Lateral dispersion is defined as the ratio between the distance separating the two extreme fall paths (as seen looking at the face of the slope) and the length of the slope (Azzoni and de Freitas 1995). According to Crosta and Agliardi (2004) the factors that control lateral dispersion are classified in three groups: macro-topography factors, factors related to the overall slope geometry; micro-topography factors controlled by the slope local roughness; and dynamic factors, associated with the interaction between slope features and block dynamics during bouncing and rolling. Assessing the results of an experimental investigation, Azzoni and de Freitas (1995) commented that the dispersion is generally in the range of 10% to 20%, regardless of the length of the slope and that steeper slopes present smaller dispersion. Agliardi and Crosta (2003) calculated lateral dispersion to be up to 34%, via high-resolution numerical models on natural rough and geometrically complex slopes.

Lateral dispersion cannot be defined from the actual rockfall event in Ponti since only one path is available. Using the simulated trajectories from RockyFor3D, which are in the 3d space (Figure 15), a lateral dispersion of approximately 60% is shown in the middle of the distance between detachment point and the house. This is significantly higher compared to the findings of Azzoni and de Freitas (1995) and Agliardi and Crosta (2003). Moreover, based on the actual event and intuition, the lateral dispersion computed by RockyFor3D is extremely pronounced and most likely due to the topography effect of the area of detachment. Specifically the origin of the rock block is located practically on the ridgeline, facilitating the deviation of the rock fall trajectory from the slope line. Examining Figure 15, it is notable that the rock paths are severely affected by topography. Therefore, assessing lateral dispersion seems to be a case specific task.

Asteriou & Tsiambaos (2016) defined deviation (e) as the dihedral angle between the pre- and post-impact planes that contain the trajectory. They found that deviation is controlled by the direction difference $\Delta\varphi$, the slope inclination and the shape of the block. For a parallel impact (i.e. $\Delta\varphi=0^0$) a spherical block presents significantly less deviation compared to a cubical. Additionally, deviation is equally distributed along the post-impact direction and reduces as the slope's inclination increases. On oblique impacts the block's direction after impact changes towards the aspect of slope and as $\Delta\varphi$ increases this trend becomes more pronounced.

Figure 16 presents deviation as a function of direction difference. It is noted that for parallel impacts deviation is also equally distributed along the post-impact direction. As direction difference increases, deviation becomes positive, which means that the change of direction is following the direction of slope’s aspect. These findings are in line with trends described by Asteriou & Tsiambaos (2016), but the deviation of the actual trajectory is significantly lower. This can be attributed to the different conditions (i.e. block shape, slope material, slope roughness, incident velocity and angle, and scale) between the experimental program conducted by Asteriou & Tsiambaos (2016) and the Ponti rockfall event.

7. Discussion - conclusions

UAV-enabled reconnaissance was successfully used for the identification of the origin of the detached rock, the rockfall trajectory and the impact points on the slope, emphasizing on the motion types of the trajectory (rolling and bouncing sections). A UAV with an ultra-high definition (UHD) camera was deployed to reach the inaccessible, steep and partly vegetated uphill terrain. A high-resolution orthophoto of the rockfall trajectory and a 10 cm DSM was prepared, which formed the basis for an analytical 2D kinematic analysis and a comparison with the outcomes of 2D and 3D rockfall analysis software.

The initial velocity of the detached rock was estimated based on site conditions and amplification of the ground acceleration due to topography. It was found that the estimation of the initial velocity of the blocks plays a significant role in the accurate re-production of the rockfall trajectory.

Based on the analytical analysis performed, it was found that the coefficients of restitution cannot be directly connected to the material type, nor can be considered constants. The impact angle seems to pose a consistent effect on normal COR, which has been observed also in other recent relevant studies, but has not been incorporated yet on analysis models.

It was proven impossible to replicate the actual trajectory of the rock fall by performing a 2D rockfall analysis with the set of parameters recommended by the developers revealing some limitations in the present formulations. In an attempt to match the actual rock path to the analysis output, the friction angle of the limestone slope was considered equal to zero. However, the falling rock still rolled on the slope and stopped much earlier than its actual runout distance while the impacts on the ground in the bouncing section of the trajectory were considerably different in number and in location compared to the actual ones.

Using the 3D analysis software, some rock trajectories better approximated the actual trajectory using the suggested values by the software developers, indicating that the 3D analysis can be more accurate than the 2D analysis.

Based on the aforementioned analyses it becomes evident that engineering judgement and experience must accompany the usage of commercial rockfall software in order to acquire realistic paths. One should never blindly use the suggested set of parameters since field performance can differ significantly, as demonstrated by this case study.

References

1. Agliardi F, Crosta GB (2003) High resolution three-dimensional numerical modelling of rockfalls. International Journal of Rock Mechanics and Mining Sciences 40:455-471. doi: 10.1016/S1365-1609(03)00021-2
2. Asteriou P, Saroglou H, Tsiambaos G (2012). Geotechnical and kinematic parameters affecting the coefficients of restitution for rock fall analysis. International Journal of Rock Mechanics and Mining Sciences 54:103-113. doi:10.1016/j.ijrmms.2012.05.029.
3. Asteriou P and Tsiambaos G. (2016). Empirical Model for Predicting Rockfall Trajectory Direction. Rock Mechanics and Rock Engineering 49.3, pp. 927–941.

4. Azzoni A, de Freitas MH (1995). Experimentally gained parameters, decisive for rock fall analysis. Rock Mechanics and Rock Engineering 28:111-124. doi: 10.1007/BF01020064

5. Buzzi O, Giacomini A, Spadari M (2012) Laboratory investigation on high values of restitution coefficients. Rock Mechanics and Rock Engineering 45:35-43

6. Crosta GB, Agliardi F (2004) Parametric evaluation of 3D dispersion of rockfall trajectories. Natural Hazards and Earth System Science 4:583-598. doi:10.5194/nhess-4-583-2004

7. Descoeudres F, Zimmermann TH. Three-dimensional dynamic calculation of rockfalls. In: Proceedings of the 6th International Congress on Rock Mechanics. Montreal; 30 August -3 September 1987. p. 337–42.

8. Dorren, L.K.A., 2012. Rockyfor3D (v5.1) revealed - Transparent description of the complete 3D rockfall model. ecorisQ paper, 31 p.

9. Ganas, A., Briole, P., Papathanassiou, G., Bozionelos, G., Avallone, A., Melgar, D., Argyrakis, P., Valkaniotis, S., Mendonidis, E., Moshou, A. and Elias, P. (2015). A preliminary report on the Nov 17, 2015 M=6.4 South Lefkada earthquake, Ionian Sea, Greece, Report to EPPO, December 4 2015.

10. Ganas A., Elias P., Bozionelos G., Papathanassiou G., Avallone A., Papastergios P. Valkaniotis S., Parcharidis I., Briole P. (2016). Coseismic deformation, field observations and seismic fault of the 17 November 2015 M = 6.5, Lefkada Island, Greece earthquake. Tectonophysics 687, pp. 210–222.

11. Giani GP. Rock Slope Stability Analysis. Rotterdam: Balkema A.A; 1992.

12. Giacomini A, Thoeni K, Lambert C, Booth S, Sloan SW (2012) Experimental study on rockfall drapery systems for open pit highwalls. International Journal

of Rock Mechanics and Mining Sciences 56:171-181. doi:10.1016/j.ijrmms.2012.07.030

13. Ferrari F, Giani GP, Apuani T (2013) Why can rockfall normal restitution coefficient be higher than one? Rendiconti Online Societa Geologica Italiana 24

14. Heidenreich B (2004) Small- and half-scale experimental studies of rockfall impacts on sandy slopes. Dissertation, EPFL.

15. ITSAK (2016). Preliminary presentation of the main recording of ITSAK – OASP accelerometer network in Central Ionian. Earthquake M6.4 17/11/2015. Thessaloniki, 11 pp.

16. Karakostas, V. G., Papadimitriou, E. E., and Papazachos, C. B. 2004. Properties of the 2003 Lefkada, Ionian Islands, Greece, Earthquake Seismic Sequence and Seismicity Triggering. Bulletin of the Seismological Society of America, 94 (5), 1976–1981, October 2004

17. Manousakis J., Zekkos D., Saroglou H., Clark M. (2016). Comparison of UAV-enabled photogrammetry-based 3D point clouds and interpolated DSMs of sloping terrain for rockfall hazard analysis. Proc. Int. Archives of the Photogrammetry, Remote Sensing and Spatial Information Sciences, Vol. XLII-2/W2, p. 71-78.

18. Marinos P, Tsiambaos G., 2002. Earthquake triggering rock falls affecting historic monuments and a traditional settlement in Skyros Island, Greece. Proc. of the Int. Symposium: Landslide risk mitigation and protection of cultural and natural heritage, Kyoto, Japan, pp. 343-346.

19. Mavrouli O., Corominas J., Wartman J. (2009). Methodology to evaluate rock slope stability under seismic conditions at Sol`a de Santa Coloma, Andorra. Nat. Hazards Earth Syst. Sci., 9, 1763–1773.Micheletti N., Chandler J., Lane

S., 2015. Structure from Motion (SfM) Photogrammetry. British Society for Geomorphology. *Geomorphological Techniques*, Chap. 2, Sec. 2.2 (2015)

21. Papathanassiou, G., Valkaniotis, S., Ganas, A. and Pavlides, S. 2012. GIS-based statistical analysis of the spatial distribution of earthquake-induced landslides in the island of Lefkada, Ionian Islands, Greece, Landslides, Journal of the International Consortium on Landslides,DOI 10.1007/s10346-012-0357-1
22. Papazachos B.C., Papadimitriou E.E., Kiratzi A.A., Papazachou C.B., Louvari E.K. 1998. Fault plane solutions in the Aegean sea and the surrounding area and their tectonic implication. Bull Geof Teor Appl 39(3), 199–218.
23. Paronuzzi P. (2009) Field Evidence and Kinematical Back-Analysis of Block Rebounds: The Lavone Rockfall, Northern Italy. *Rock Mech Rock Eng*, 42:783–813
24. Richards LR, Peng B, Bell DH (2001) Laboratory and field evaluation of the normal Coefficient of Restitution for rocks. Proceedings of ISRM Regional Symposium EUROCK2001:149-155
25. RocScience, 2004. Rocfall Manual.
26. Rondoyanni Th., Mettos A., Paschos P., Georgiou Ch. 2007. Neotectonic map of Greece, scale 1:100.000, Lefkada sheet. I.G.M.E., Athens.
27. Saroglou, H. 2013. Rockfall hazard in Greece. Bulletin of the Geological Society of Greece, vol. XLVII, no3, 1429-1438.
28. Saroglou, H., Marinos, V., Marinos, P., Tsiambaos, G. 2012. Rockfall hazard and risk assessment: an example from a high promontory at the historical site of Monemvasia, Greece. Natural Hazards and Earth System Sciences, 12, 1823–1836. doi:10.5194/nhess-12-1823-2012.

29. Snavely N., Seitz S.N., Szeliski R., 2008. Modeling the world from internet photo collections. *International Journal of Computer Vision* 80: 189-210.

30. Spadari M, Giacomini A., Buzzi O., Fityus S., Giani G.P.(2011). In situ rockfall testing in New South Wales, Australia. Int J Rock Mech Mining Sci, 49, pp. 84–93.

31. Volkwein, A., Schellenberg, K., Labiouse, V., Agliardi, F., Berger, F., Bourrier, F., Dorren, L. K. A., Gerber, W., and Jaboyedoff, M., 2011. Rockfall characterisation and structural protection – a review, Nat. Hazards Earth Syst. Sci., 11, 2617–2651, doi:10.5194/nhess-11-2617-2011.

34. Westoby M.J., Brasington J., Glasser N.F., Hambrey M.J., Reynolds J.M., 2012. 'Structure-from-Motion' photogrammetry: A low-cost, effective tool for geoscience applications. *Geomorphology* 179 (2012) 300-314.

35. Wyllie, D. C. (2014). Calibration of rock fall modeling parameters. International Journal of Rock Mechanics and Mining Sciences 67: 170-180

36. Zekkos D., Clark M., Cowell K., Medwedeff W., Manousakis J., Saroglou H. Tsiambaos G. (2017). Satellite and UAV-enabled mapping of landslides caused by the November 17th 2015 M_w 6.5 Lefkada earthquake. Proc. 19th Int. Conference on Soil Mechanics and Geotechnical Engineering, Seoul 2017 (accepted for publication).

TABLES

Table 1. Accelerometer recordings

Component	Acceleration (cm/sec^2)	Velocity (cm/sec)	Displacement (cm)
NS-comp	363	59.3	21.27
EW-comp	327	34.1	14.01
Z-comp	256	17.7	6.56

Table 2. Impact points characteristics

Impact point	X (m)	Y (m)	app_dip (^{0})	Δφ (^{0})	e (^{0})
1	287.63	338	39.0	0	0
2	298.38	329.68	16.3	33	0
3	305.48	324.5	27.9	27	-1
4	321.54	314.83	41.0	11.6	0.5
5	365.34	287.6	30.4	11.9	0.3
6	373.32	284.85	39.7	10.6	1.8
7	425.1	261.64	14.7	6.6	-1.3
8	464.43	251.13	18.4	33.3	0.8
9	472.06	248.81	14.0	19.1	2.3
10	495.29	243.81	7.5	52.3	0.9
11	515.31	240.8	7.9	51	0.6
12	535.56	238.31	9.1	46.7	3
13	562.11	232.22	8.7	47.3	2.1
14	605.51	211.12	16.9	25.6	-1.7
15	619.1	204.48	27.1	4.6	-3
16	639.13	196.96	21.2	8	4.7
17	662.41	184	23.3	28.5	5.2
18	688.4	169.3	27.4	0.3	-2.5
19	712.23	157.67	25.4	0.5	0.1
20	745.28	143.16	21.9	0.5	-0.1
21	762.9	137.01	22.0	0.7	2
22	789.23	125.98	21.6	1.4	-0.8
23	801.53	132.75	8.4	0.2	0.1

Table 3. Parabolic paths characteristics for the minimum release velocity

Segment	Δx(m)	Δy (m)	θ_{cr} (^{0})	$v_{r,min}$	v_{impact}	a_i	v_{COR}	n_{COR}	t_{COR}
1-2	10.75	-8.33	26.8	7.19	13.19	44.5	0.55	0.71	0.31
2-3	7.1	-5.18	25.7	5.95	9.51	27.8	0.63	0.90	0.53
3-4	16.07	-9.66	31.5	9.45	12.68	9.6	0.75	3.86	0.38
4-5	43.79	-27.23	27.7	15.46	23.13	23.3	0.67	1.57	0.26
5-6	7.98	-2.75	35.7	7.47	10.49	14.9	0.71	2.52	0.30
6-7	51.78	-23.21	34.8	18.15	21.61	31.7	0.84	1.54	0.26
7-8	39.33	-10.5	35.9	17.23	24.01	36.1	0.72	0.94	0.56
8-9	7.63	-2.32	35.9	7.45	10.54	41.1	0.71	0.87	0.55
9-10	23.23	-5	40.5	13.58	13.12	30.7	1.03	1.65	0.70
10-11	20.02	-3.01	41.1	13.00	11.57	24.2	1.12	2.06	0.82
11-12	20.25	-2.49	40.9	13.26	11.22	17.6	1.18	2.94	0.82
12-13	26.55	-6.1	38.0	14.40	14.25	28.5	1.01	1.55	0.78
13-14	43.41	-21.1	32.9	16.33	25.70	40.9	0.64	0.64	0.63
14-15	13.59	-6.64	30.7	9.13	12.81	25.1	0.71	1.24	0.53
15-16	20.03	-7.52	33.8	11.67	15.42	29.8	0.76	1.33	0.42
16-17	23.27	-12.96	31.9	11.59	15.89	28.5	0.73	1.22	0.50
17-18	25.99	-14.7	29.9	12.20	20.11	30.9	0.61	0.95	0.42
18-19	23.83	-11.63	32.2	12.08	17.10	27.9	0.71	1.30	0.40
19-20	33.05	-14.51	33.6	14.55	20.62	32.1	0.71	1.14	0.43
20-21	17.62	-6.15	34.5	11.08	11.99	18.4	0.92	2.44	0.54
21-22	26.33	-11.03	35.1	13.11	16.33	27.3	0.80	1.47	0.49
22-23	12.3	6.77	58.1	14.30	13.97	48.9	1.02	1.34	0.28

Table 4. Restitution parameters for Rockyfor3D

Geological formation/ other	Mean n_{COR}	MOH			Soil type (Rockyfor3D)
		rg70	rg20	rg10	
Scree (Ø < ~10 cm), or medium compact soil with small rock fragments	0.33	0.03	0.05	0.05	3
Talus slope (Ø > ~10 cm), or compact soil with large rock fragments	0.38	0.05	0.1	0.2	4
Talus with fallen boulders	0.42	0.15	0.15	0.2	4.1
Bedrock with thin weathered material	0.43	0	0.05	0.1	5
Asphalt road	0.35	0	0	0	7

FIGURES

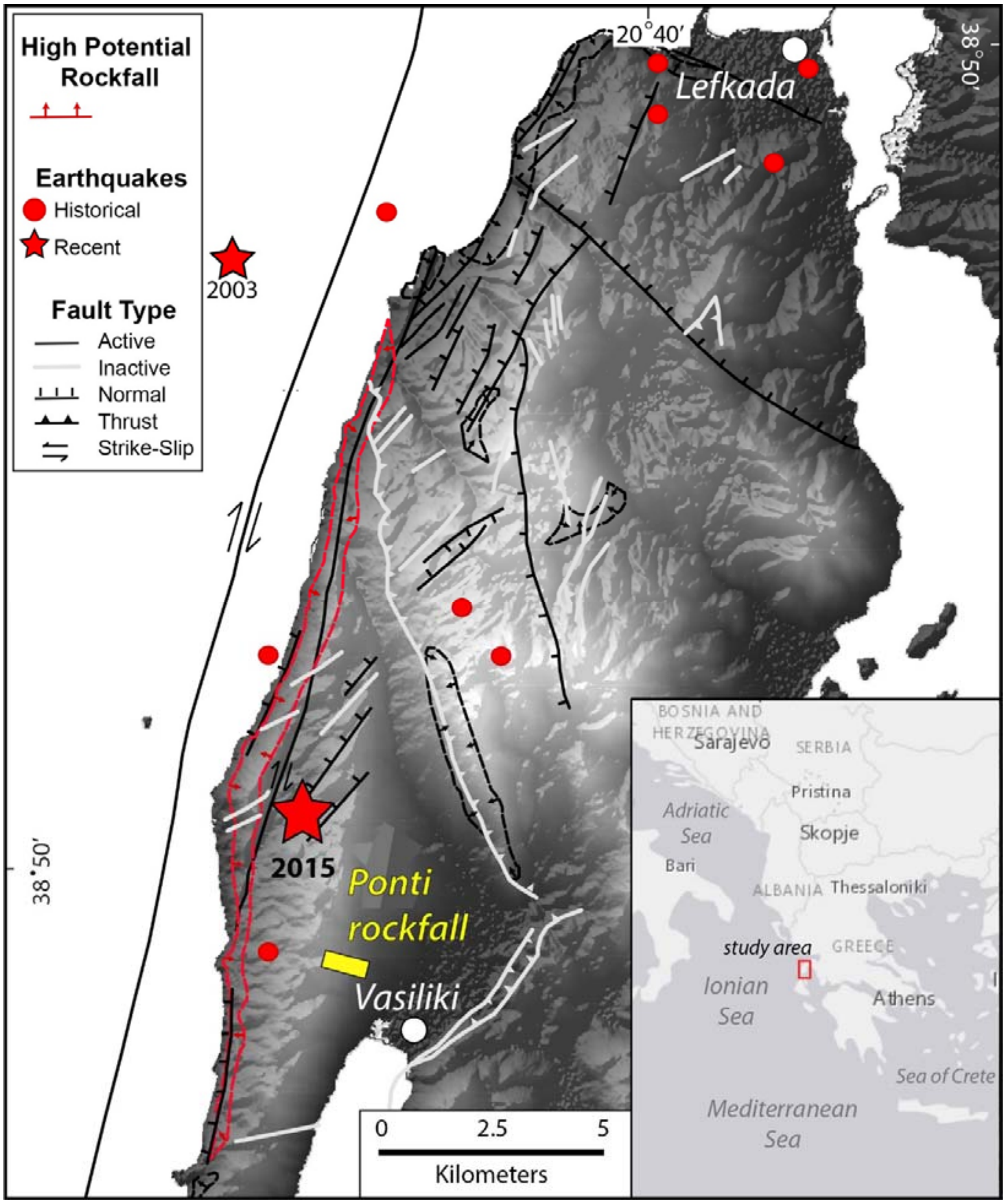

Figure 1. Map of Lefkada Island, Greece with location of study site (Ponti) and epicenters of recent earthquakes (stars) in 2003 (M_w6.2) and 2015 (M_w6.5), as well as historical ones (circles) Map also shows faults and high potential rockfall areas as identified by Rondoyanni et al. (2007).

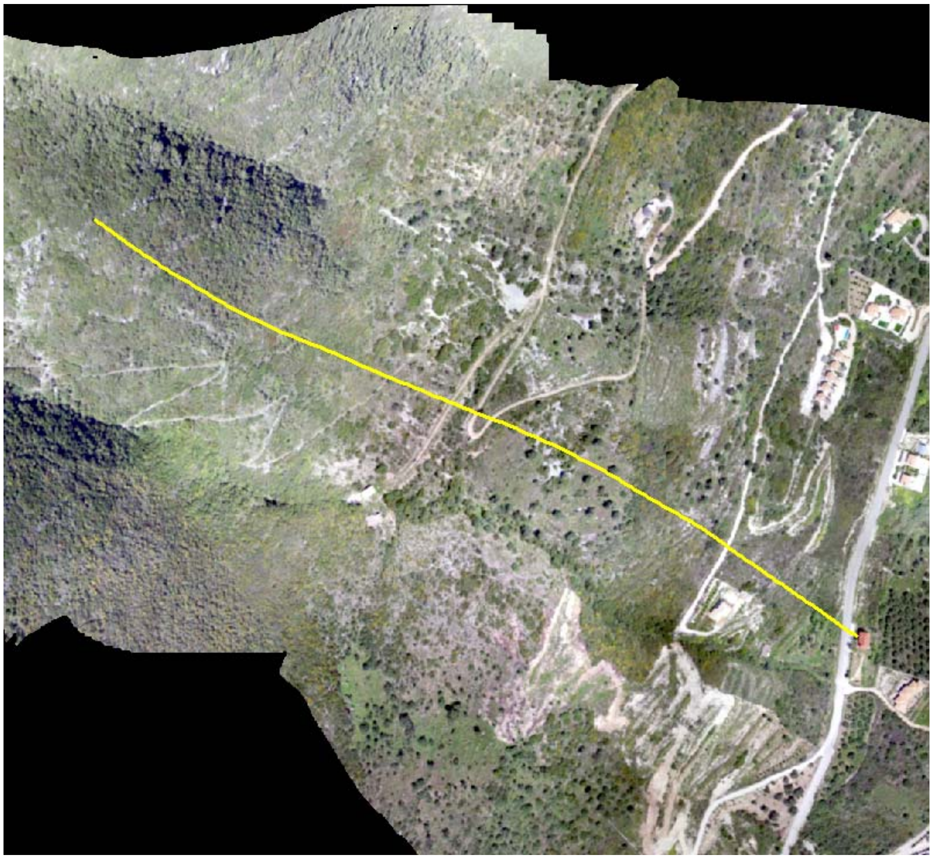

Figure 2. Orthophoto of study site. The total length of the trajectory shown with a yellow line, is 800 m.

Figure 3. Impact of rock on house in Ponti, Lefkada, Greece.

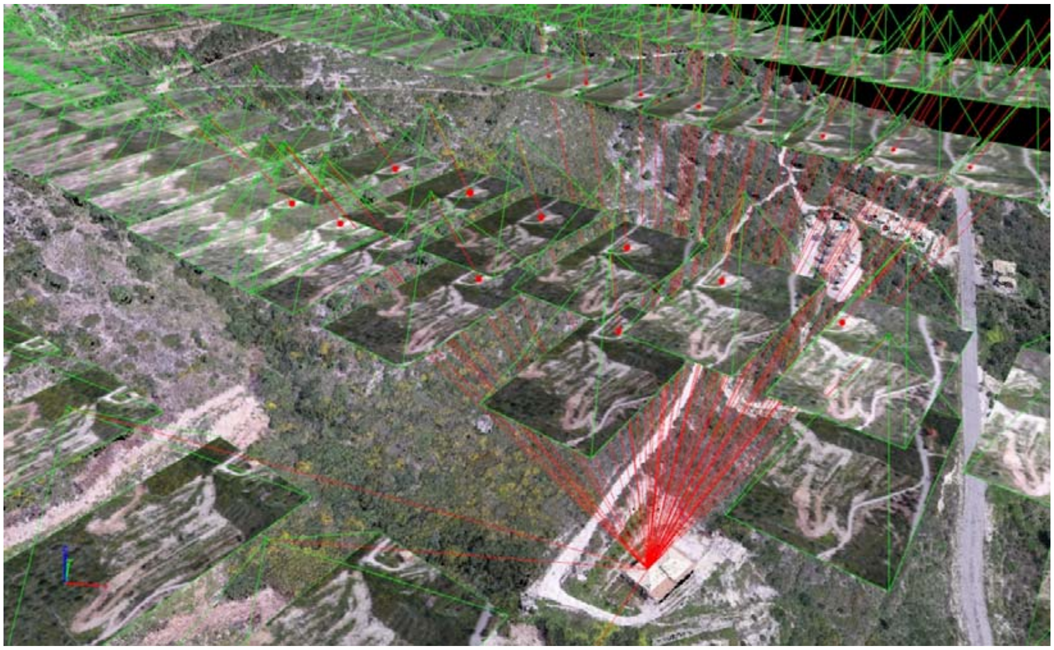

Figure 4. Shematic illustrating the overlap between pictures in the study site using SfM methodology.

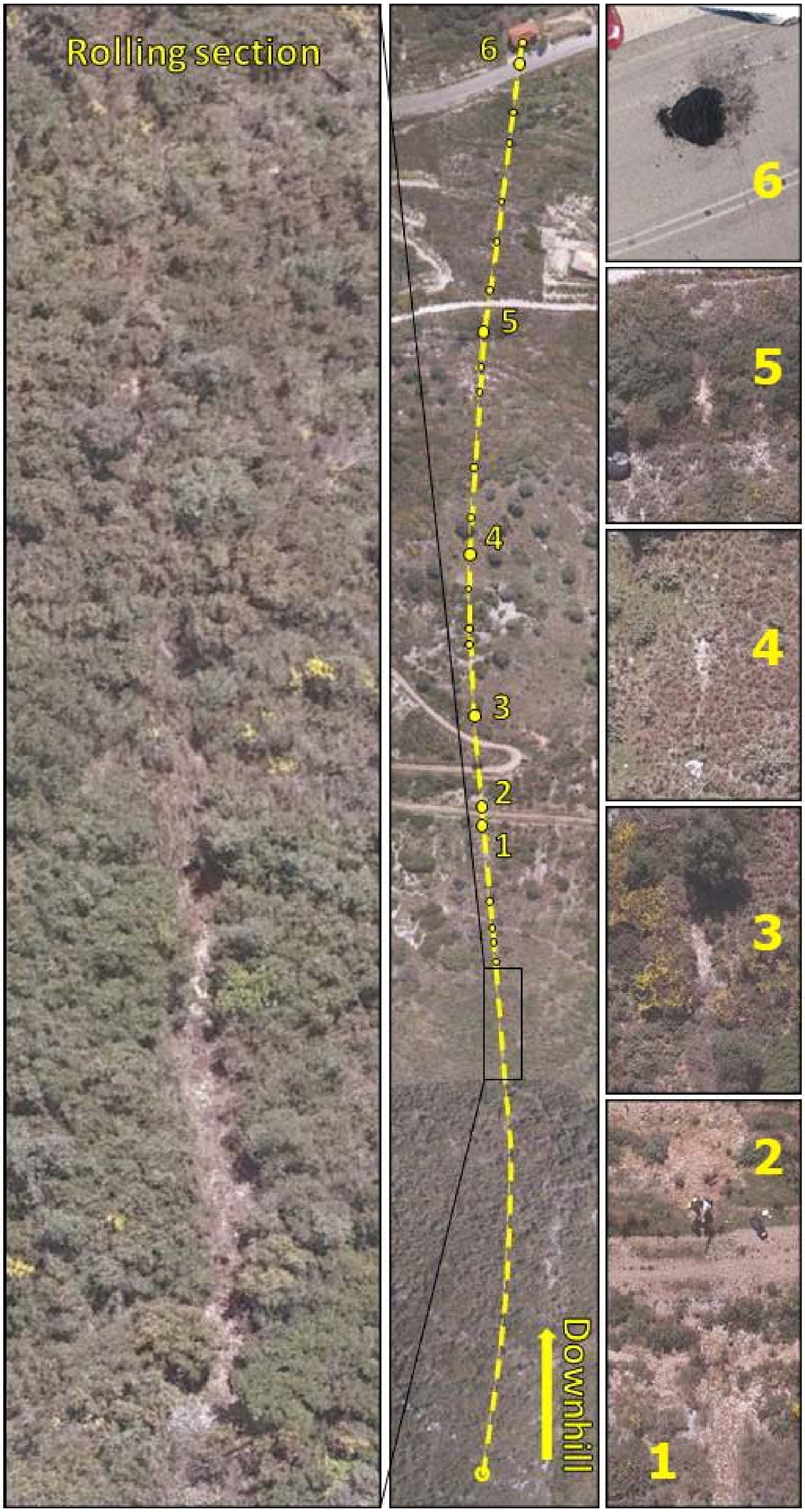

Figure 5. Top view orthophoto denoting rolling section, bouncing positions and indicative close-ups of impact points.

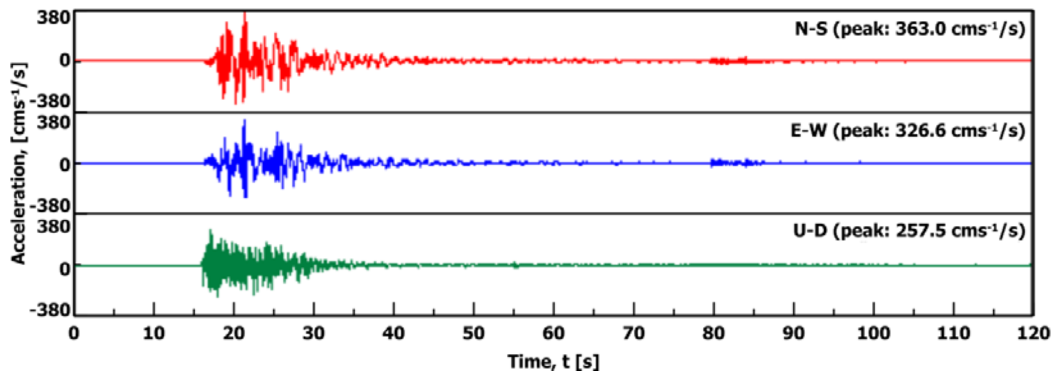

Figure 6. Acceleration recording at Vassiliki site (ITSAK, 2016)

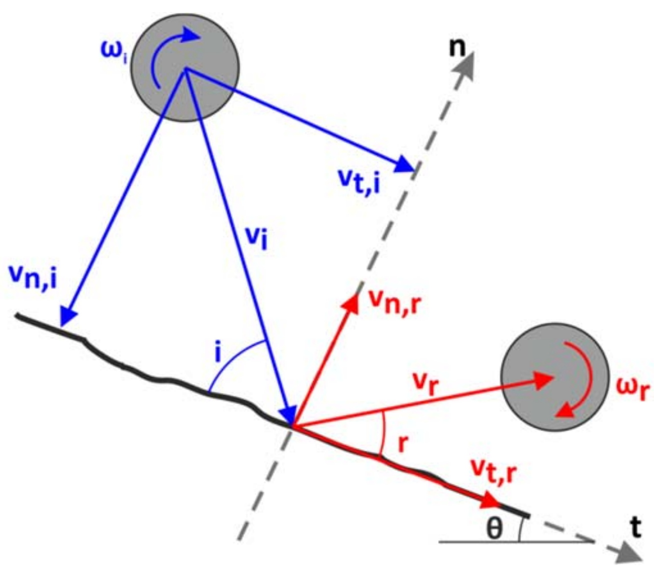

Figure 7. Coefficients of restitution

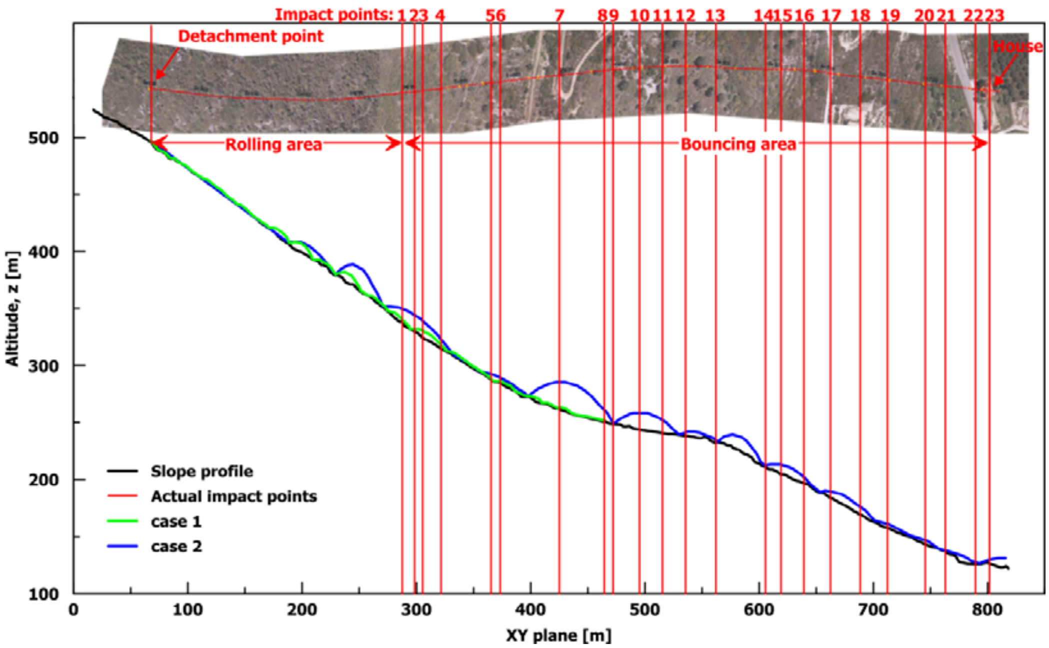

Figure 8. Plan view and cross section along block's path (units in m); 2D rockfall trajectory analysis results are plotted with green and blue line

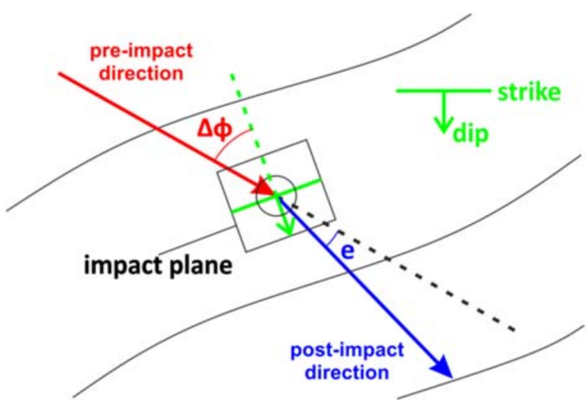

Figure 9 : Out of plane geometry

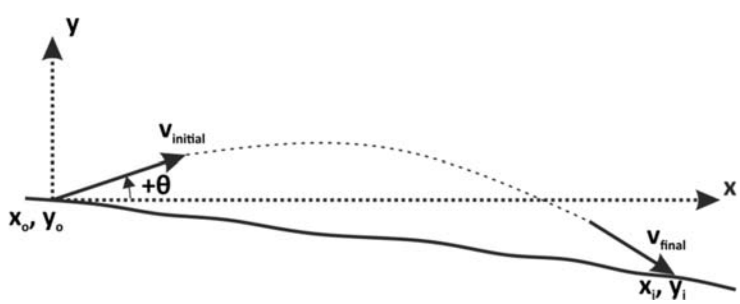

Figure 10. Parabolic segment

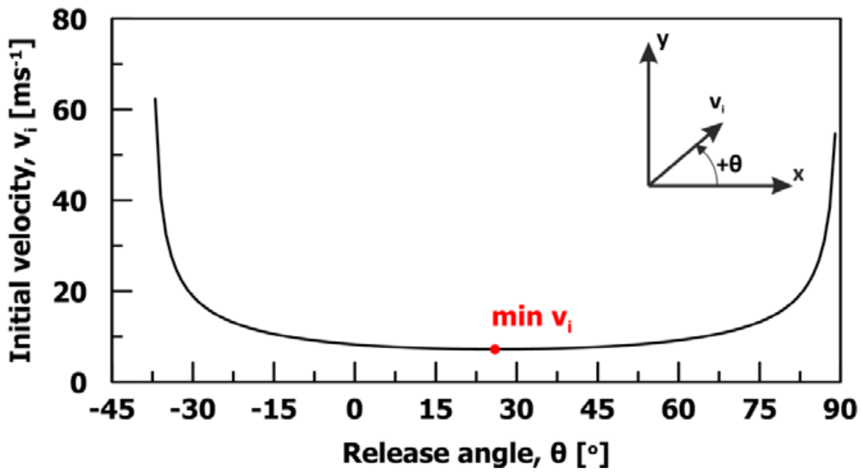

Figure 11. Release angle versus initial velocity for the first parabolic section (δx=10.75m, δy=8.33m)

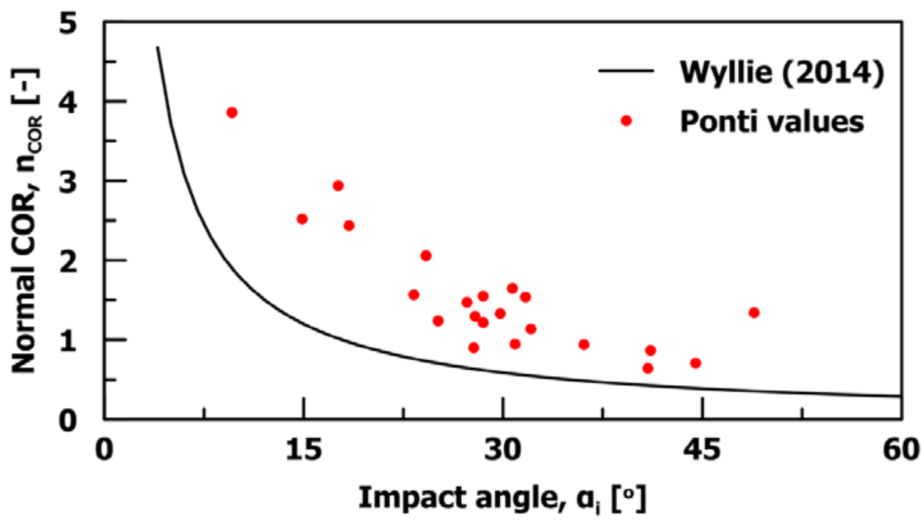

Figure 12. Normal COR versus impact angle

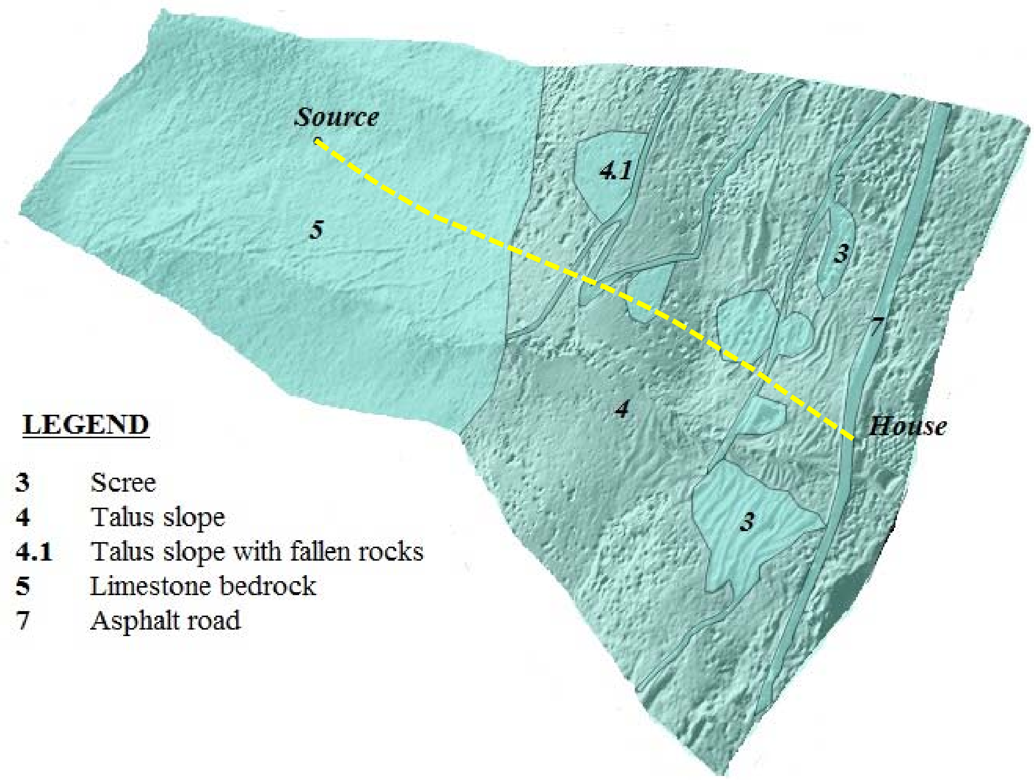

Figure 13. Soil types for 3D rockfall analysis (according to Rockyfor3D). Yellow path of trajectory is 800 m.

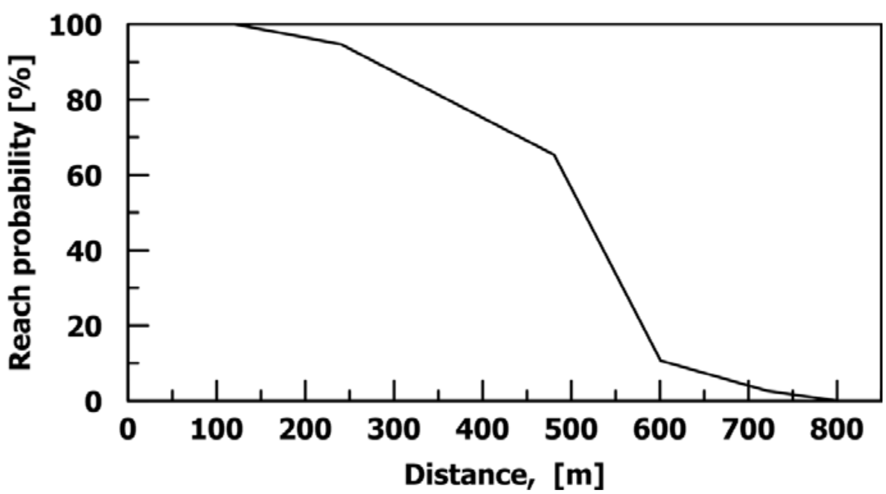

Figure 14. Reach probability graph calculated from 3D rockfall analysis

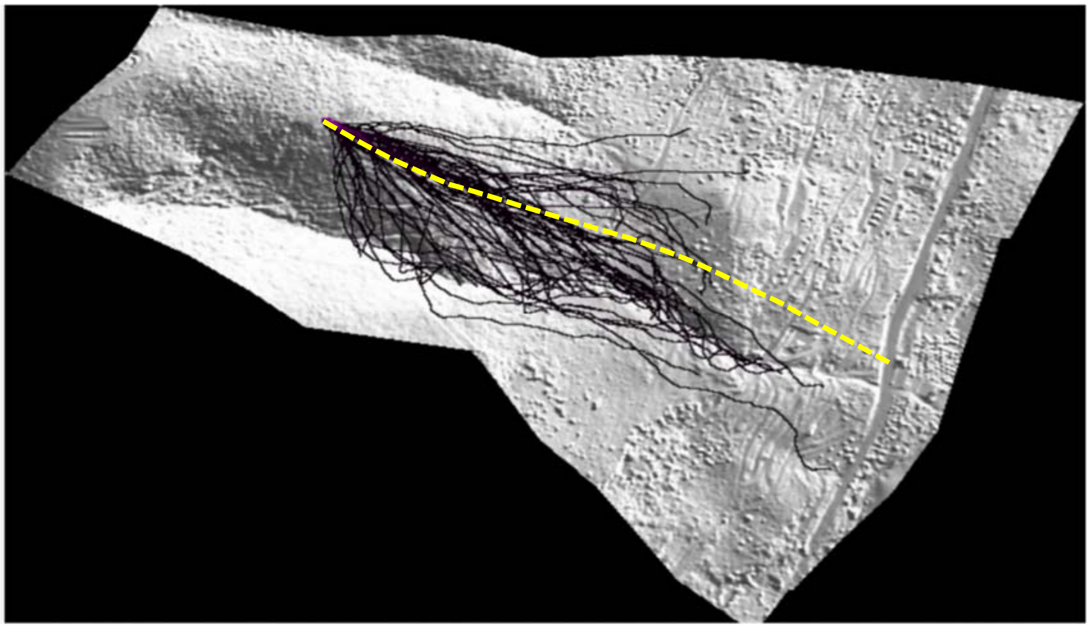

Figure 15. 3D trajectory analysis (from RockyFor3D analysis). Yellow line shows the actual trajectory. Black lines show the simulated trajectory.

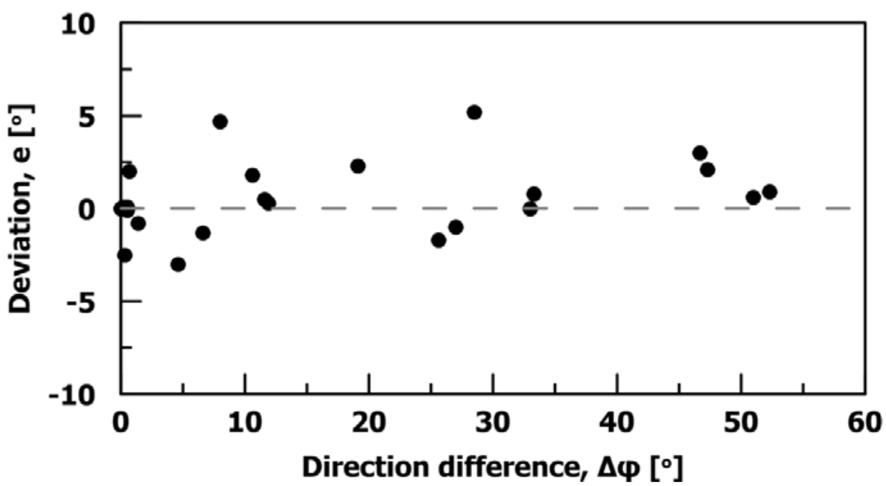

Figure 16. Deviation as a function of direction difference.